Analysis of the warm absorber in NGC 6814

by

Rebecca Hamel

A THESIS SUBMITTED IN PARTIAL FULFILMENT OF
THE REQUIREMENTS FOR THE DEGREE OF

BACHELOR OF SCIENCE

in

Honours Astrophysics

(Department of Astronomy and Physics, Dr. Luigi C. Gallo supervising faculty)

.....
.....
.....
.....
.....

SAINT MARY'S UNIVERSITY

April 22, 2024

Abstract

Analysis of the warm absorber in NGC 6814

by *Rebecca Hamel*

submitted on April 22, 2024:

NGC 6814, a Seyfert 1.5 Active Galactic Nucleus (AGN) at redshift z = 0.00522, is a compelling object to study due to its high X-ray variability and the presence of photoionized gas outflows. In 2016, a rapid occultation event, indicative of the presence of a highly ionized absorbing gas, was detected in NGC 6814, presenting a unique opportunity to investigate the properties, size, and location of the eclipsing gas. The primary objective of this work is to probe the warm absorber in NGC 6814 using high-resolution spectra from 2021, comparing the properties of the warm absorber with those from the obscuring gas observed in 2016. This analysis aims to unveil insights into the origin of the eclipsing gas and provide further details on the properties and kinematics of the central region of NGC 6814. This work reveals that two warm absorbing models with similar velocities but varying ionisations and densities are statistically required to fit the absorption features in the spectrum, with some features remaining unfitted. A picture can be drawn of the warm absorption system in NGC 6814, where both warm absorbing clouds are a part of the same medium moving outwards at a velocity of $\approx$ 2500 km s^{-1}, or that the two warm absorbers are describing an ionisation and density gradient within the same cloud.

Contents

Contents iii

List of Figures v

List of Tables vii

1 Introduction 1

1.1 Active Galactic Nuclei 1

1.1.1 The X-ray Emitting Region 2

1.1.2 The Surrounding Region of the AGN 7

1.1.3 Warm Absorbers 8

1.1.4 Types of AGN 10

1.2 Observing AGN in X-rays 10

1.2.1 X-ray Telescopes 11

1.2.2 Flux Light Curves 12

1.2.3 High Resolution Spectra 12

1.3 NGC 6814 16

1.3.1 2016 Observations 17

1.3.2 The Nature of the Obscuring Material 17

1.3.3 2021 Observations 18

1.4 Motivation 19

2 Observations 21

3 Line Search 26

3.1 Methodology 26

3.2 Line Identification 27

4 Physical Models 31

4.1 Warm Absorption Models (xabs) 31

4.2 2021 RGS Fit 32

5 Discussion 39

5.1 Comparison of the 2021 RGS Model to the 2016 RGS Data 39

5.2 A Picture of the Warm Absorption System in NGC 6814 . 42

6 Conclusions 44

Bibliography 46

List of Figures

1.1 The Central Region of AGN 5

1.2 The Combined Observed X-ray Spectrum of AGN 6

1.3 A Simple Illustration of the AGN Region Depicting Scales and Main Components 9

1.4 He-Like Ions Energy Levels Scheme and X-ray Lines 14

1.5 Temperature and Density Diagnostic Plots for Helium-Like Oxygen . 15

1.6 The Light Curve, Hardness Ratio Curve, and Schematic of the 2016 NGC 6814 Transient Eclipsing Event 18

2.1 The Unfitted 2021 XMM-Newton RGS Spectrum 22

2.2 The Unfitted 2016 XMM-Newton Eclipsed RGS Spectrum 23

2.3 The Unfitted 2016 XMM-Newton un-Eclipsed RGS Spectrum 23

2.4 The Unfitted 2016 XMM-Newton Full RGS Spectrum 24

2.5 The Unfitted 2021 Chandra HETG Spectrum 25

3.1 The Line Search Conducted on the 2021 XMM-Newton RGS Data Range of 7-20 Å 29

3.2 The Line Search Conducted on the 2021 XMM-Newton RGS Data Range of 20-28 Å 30

4.1 The Step Grid Search for WA1 33

4.2 The Step Grid Search for WA2 35

4.3 The Transmission Curves of Components in the Fitted Model on the XMM-Newton 2021 RGS Spectrum 37

4.4 The Modelled 2021 XMM-Newton RGS Spectrum 38

5.1 The Modelled 2016 XMM-Newton RGS Spectrum 40

5.2 A Picture of the Warm Absorption System in NGC 6814 43

List of Tables

1.1 Reported Parameters of the 2016 Obscurer in NGC 6814 19

2.1 Data Information for the 2021 Observation of NGC 6814 22

3.1 Line Identification of the 2021 XMM-Newton RGS Data 28

4.1 Free Parameters of the Absorption Model for the 2021 RGS Data . . 36

5.1 Free Parameters of the Absorption Model Added to the 2016 Full RGS Data 41

Chapter 1

Introduction

Active Galactic Nuclei (AGN) are some of the most energetic and luminous objects found across the Universe. With current knowledge, technology, and observations, we can shed some light on these once elusive sources. This chapter presents an overview of AGN and examines the components within the central regions of active galaxies. It delves into the specific characteristics of NGC 6814, with a particular emphasis on the occultation event observed in 2016. Additionally, the chapter discusses the advantages of employing high-resolution spectra in the analysis of the system kinematics, providing insights into key parameters that contribute to a comprehensive understanding of various components found in AGN.

1.1 Active Galactic Nuclei

AGN are embedded within a very compact region at the centre of galaxies. Unlike normal galaxies, for which their luminosity originates from the combination of all its stellar members and their spectra are modelled by a blackbody-like shape, AGN can be many magnitudes brighter, outshining the stars of the host galaxy, and emit light across the entire electromagnetic (EM) spectrum (Gallo, 2011). Some AGN can also exhibit high flux variability, and jets, extending hundreds of thousands of light years from the centre of its galaxy. These phenomena are closely linked to the presence

of supermassive black holes (SMBHs) at the cores of galaxies (Ryden and Peterson, 2021).

It is widely accepted that at the centre of all galaxies lies a supermassive black hole, millions to billions of times more massive than the Sun (Gallo, 2011). The presence of these SMBHs is responsible for the incredible light emissions observed in some galaxies. In some cases, SMBHs begin actively accreting incredible amounts of material. As matter falls into the SMBH, it begins to accelerate at relativistic velocities, and forms an accretion disc around the black hole.

The matter closer to the SMBH moves at a higher velocity than the material further away, generating viscosity between regions of the disc, thus transferring angular momentum outward, and allowing the material to continue flowing inward (Gallo, 2011). As the gas continues to fall toward the black hole, it radiates, peaking in the ultraviolet (UV) region. Accretion is the dominant process in AGN. The following sections will dive deeper in the various regions of the central engine of AGN.

1.1.1 The X-ray Emitting Region

Another important feature observed in AGN is strong X-ray emission, but the temperatures required to account for this emission cannot be reached within the accretion disc (Gallo, 2011). From variability studies, we can infer the origins of the X-ray emitting region. Isotropic emitters can only vary as fast as the time it takes for light to travel across their region, allowing us to constrain the size of the X-ray emitting region using the duration of variability events. Depending on the mass of the SMBH,

the exact size of this region will vary. However, the regions are extremely compact, and unresolved even for the nearest AGN (Gallo, 2011). To understand the X-ray emitting region, we must rely on indirect observing methods such as spectral and timing analysis. These methods will be discussed further in Section 1.2, where we discuss the application of spectral and timing analysis to understand the complexities of the X-ray emitting region. There are two regions in AGN which emit X-rays: the primary emitter and the reflection from the accretion disc.

The Primary Emitter

Originating from the inner region of the SMBH and the accretion disc, the primary X-ray emitting region, also known as the corona, plays a crucial role in AGN emissions. The temperature of the electron gas is on the order of 10^9 K and likely originates from electrons pulled away from the accretion disc through the reconnection of magnetic fields (Gallo, 2011). UV photons from the accretion disc collide with the hot electrons in the corona, gaining energy through multiple interactions (Figure 1.1). This process, known as Comptonization or inverse Compton scattering, results in the emergence of X-rays from the gas. This extended atmosphere of hot electrons leads to an emission that is uniform in all directions, referred to as isotropic emission (Figure 1.1). It is characterized by a power-law spectrum with a sharp cut-off at high energies (Figure 1.2).

The Reflection Spectrum

As the corona acts as an isotropic emitter, a portion of the X-rays emitted will be directed towards the accretion disc, giving rise to a secondary X-ray emission component known as the reflection spectrum (Figure 1.1). The remaining bound electrons found in heavier elements in the accretion disc will eventually transfer to lower excited states. This process releases photons in a fluorescence process (Gallo, 2011). This photon emission contributes to the secondary X-ray emission component that is sometimes observed in AGN spectra as an excess at both higher and lower energies (Figure 1.2. At higher energies, the reflection spectrum will not be visible as there are no longer any bound electrons left at the surface of the accretion disc (Gallo, 2011). The reflection spectrum provides valuable information on the ionization, composition, and dynamics of the accretion disc.

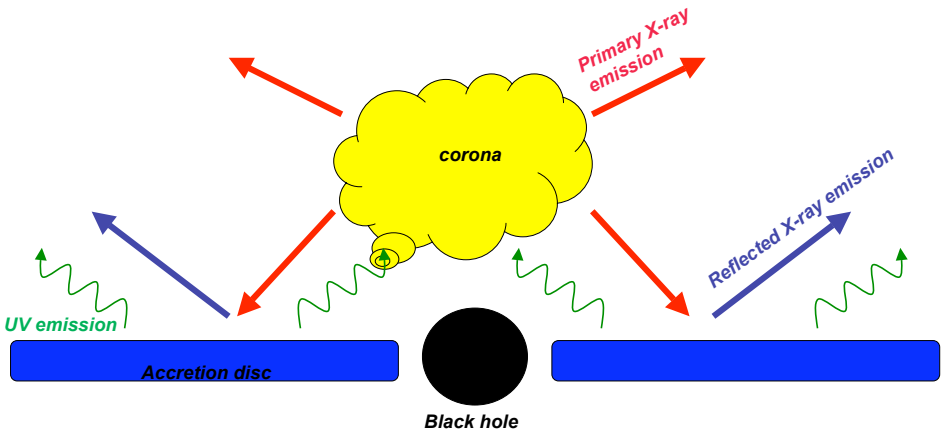

Figure 1.1: A depiction of the central region of an AGN where the X-rays are generated. Taken from Gallo (2011). The hot corona emits isotropically, thus resulting in a part of its X-rays being directed towards the accretion disc, and reflected back outwards. The accretion disc also shines mainly in the uv band, thus emitting UV photons as well.

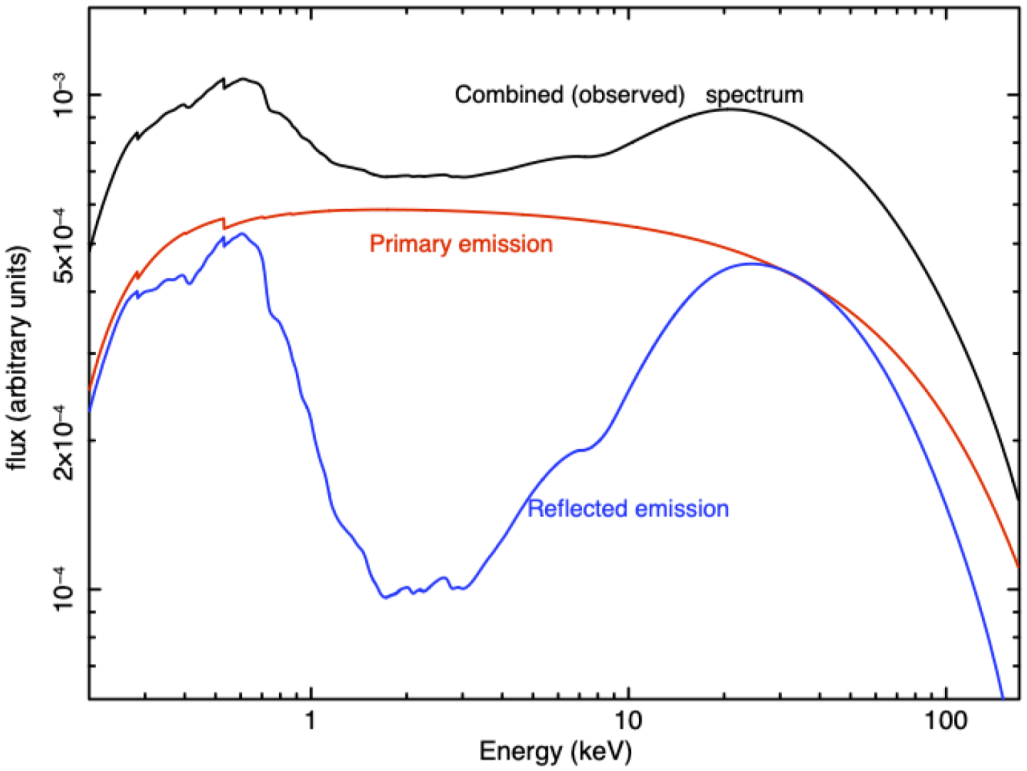

Figure 1.2: The combined observed X-ray spectrum of an AGN and the components contributing to each part of the spectrum Taken from Gallo (2011). The primary emission (red), modelled by a power law is produced by the hot corona. The reflected emission (blue), shown as an excess at higher and lower energies in the X-ray band, originate from the accretion disc, and may or may not be present in spectra. The combined or observed spectrum (black) is the combination of both these emission components.

1.1.2 The Surrounding Region of the AGN

Given that AGN are embedded within the center of galaxies, the presence of gas clouds within their central regions is anticipated. These clouds, depending on their location and properties, will imprint distinct signatures on AGN observation. For instance, the location and properties of these clouds can manifest in specific features within AGN spectra, offering valuable insights into the dynamics and composition of the central regions (Figure 1.3).

The Obscuring Torus

At larger distances, at the dust sublimation radius, the X-ray emission from the hot corona is minimized, allowing for the formation of dust particles, resulting in the creation of a warm dust cloud known as the torus (Ryden and Peterson, 2021). The torus is optically thick to most radiation, absorbing low-energy X-rays and UV photons and re-emitting them as infrared photons (Jones et al., 2015). While the torus is a separate structure from the accretion disc, it likely lies along the same plane (Figure 1.3). This alignment, however, does not suggest a connection between the torus and the accretion disc, as they could also be unique structures.

The Broad-line Region

In proximity to the central engine, gas clouds undergo photoionization by the hot corona, and inner accretions disc (Figure 1.3). These clouds become gravitationally bound to the supermassive black hole (SMBH) and accelerated in a circular orbit at several thousands of kilometers per second. As a result, the emission features from

this gas experience significant Doppler broadening — a phenomenon where spectral lines become broader due to the motion of the emitting source (Jones et al., 2015). This led to the term 'broad-line region' (BLR) being coined to describe these high-velocity gas clouds.

The Narrow-line Region

Some clouds may extend further away from the central engine to galactic scales, and their motion is dominated by the smoothed galactic potential in that region (Figure 1.3). They move at much lower speeds, on the order of a few hundred kilometers per second. As a result, the emission features from these gas clouds are narrower than their BLR counterparts (Jones et al., 2015). In the narrow-line region (NLR) of AGN the densities are low and forbidden transitions can occur. These transitions will be discussed further in Section 1.2.3.

1.1.3 Warm Absorbers

Some AGN observations also report signs of absorption features within their X-ray spectra. These absorption features have been attributed to highly photoionized nuclear winds found at greater distances away from the central engine (Figure 1.3). These clouds of gas, referred to as warm absorbers (WA), offer a unique opportunity to probe the properties of the absorbing material such as the quantity of gas, its density, temperature, position, and velocity, using high resolution spectra (Gallo et al., 2023). The advantages of using high-resolution spectra to analyse the properties of warm absorbers will be discussed in detail in Section 1.2.

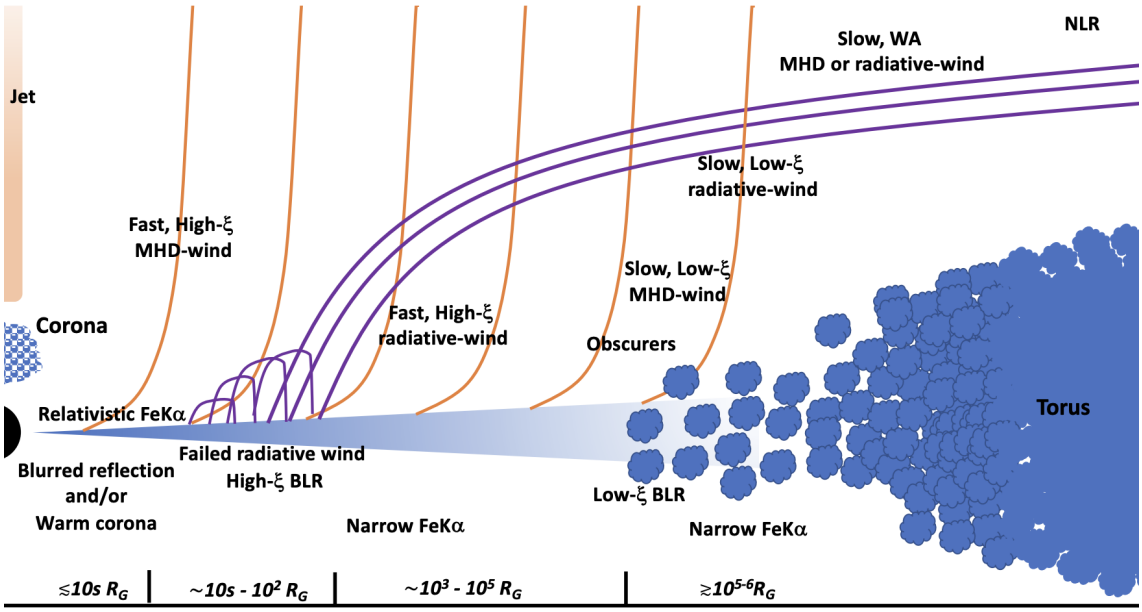

Figure 1.3: A simple illustration of the AGN region depicting the scales and main components responsible for X-ray emission. Taken from Gallo et al. (2023). The diagram showcases the relative scales, with the hot corona near the central engine, responsible for the primary X-ray emission in AGN, and the presence of the BLR. Extending further, we also find the obscuring torus, along the same plane as the accretion disc. At galactic scales, the NLR is found. WAs can exist at various scales in the AGN system.

1.1.4 Types of AGN

It is essential to recognize that AGN spectra can vary significantly. Some may exhibit absorption features, while others may not show the broad-line and narrow-line regions. However, a unified model helps explain that these seemingly different AGN structures are, in fact, the same. The observed differences depend on the direction from which the AGN is viewed relative to the torus (Jones et al., 2015).

At various lines of sight, different components of the AGN may be visible. For example, if an observer were to be observing an AGN directly through the torus, the optically thick gas and dust will obscure our view of the central engine and the broad-line region of the AGN, and we will observe a type 2 Seyfert or a type 2 quasar if its luminosity is more significant (Ryden and Peterson, 2021). On the opposite end, if we observe the AGN perpendicular to the torus, we will have a direct view of the central engine and the various components at the centre. These AGN are referred as type 1 Seyferts or type 1 quasars (Ryden and Peterson, 2021). Using this unified model, we can infer the inclination of the AGN along the line of sight and predict the components expected to appear in its spectrum.

1.2 Observing AGN in X-rays

Since the central regions of galaxies are unresolved, we must use indirect methods to observe AGN. Two common methods used to probe properties of AGN include measuring the temporal change in flux over time, offering insights into variability, as well as modelling their high-resolution spectra, providing detailed information about

the composition and dynamics.

1.2.1 X-ray Telescopes

With today's current X-ray telescopes, we are able to pierce further than ever before into the central regions of AGN, and probe the various components found within them. X-ray observatories, such as XMM-Newton[1] and Chandra[2], provide us with detailed flux curves and spectra of AGN.

XMM-Newton

The X-ray Multi-Mirror Mission (XMM-Newton) was launched in 1999 and with its three high throughput X-ray telescopes with unprecedented effective area, and an optical monitor, XMM-Newton has revolutionised our understanding of AGN.

Aboard the telescope, there are three CCD detectors - one pn-type semi-conductor and two metal oxide semi-conductors (MOS1 and MOS2), which provide both imaging and moderate spectral resolution. There are also two grating spectrometers - Reflection Grating Spectrometers called RGS 1 and 2. These two grating spectrometers achieve high resolving power over a range from 5 to 35 Å, and offer the highest spectral resolution for low-energy X-rays.

[1] https://www.cosmos.esa.int/web/xmm-newton
[2] https://chandra.harvard.edu/

Chandra

The Chandra X-ray Observatory was also launched in 1999. Featuring four pairs of mirrors and four instruments, Chandra is one of the most successful NASA missions for X-ray Astronomy.

The four instruments include: a High Resolution Camera (HRC), an Advanced CCD Imaging Spectrometer (ACIS) and two High Resolution Spectrometers - the High Energy Transmission Grating Spectrometer (HETGS) and the Low Energy Grating Spectrometer (LETGS). The HETGS can provide high spectral resolution for high energy X-rays in the range from 1 to 30 Å.

1.2.2 Flux Light Curves

A common characteristic identified in AGN is their X-ray variability. As briefly mentioned in Section 1.1, the variability period of AGN allows us to infer the size of their X-ray emitting regions. The flux can only vary as fast as it takes for light to travel across the emitting region (Gallo, 2011). Utilising this property, we can employ the light curve to constrain the radius of the inner regions of AGN, providing crucial insights into their dynamic behavior and underlying processes.

1.2.3 High Resolution Spectra

Another important tool in studying AGN is high-resolution spectra. By modelling the high-resolution spectra of AGN, we can identify various components present in the AGN, such as radiative outflows or inflows (Kaastra et al., 2014), emitting and

absorbing regions, and their parameters. These parameters, in turn, play a crucial role in determining properties such as the quantity of gas, its density, temperature, position, and velocity. Understanding these properties contributes significantly to unraveling the intricate physics governing AGN.

Column Density

The column density (N_H) serves as a diagnostic for the quantity of material present in the line-of-sight. A higher column density suggests a larger or denser cloud with more material capable of absorbing or emitting light.

Ionization Parameter

The ionization parameter (ξ) serves as a dual diagnostic for both density and position within a gas cloud. It reflects the level of ionization in the cloud, influenced by the luminosity of the primary emitter (L_{ion}), gas density (n), and its position (r). Mathematically expressed as:

$$\xi = \frac{L_{ion}}{nr^2} \qquad [\mathrm{erg\,cm\,s^{-1}}] \tag{1.1}$$

The ionization parameter offers valuable insights into the properties of the gas component such as its position. Values for the luminosity and the density can be obtained through fitting models to spectra, which can then allow us to constrain the radius at which the clouds are found.

Velocity

By assessing the redshift or blueshift of features within a specific component of the spectrum, we can deduce the velocity of the associated gas. This analysis allows us to determine whether the gas is inflowing (redshift) or outflowing (blueshift) with respect to the rest frame of the AGN.

Line Ratios

A persistent challenge in AGN spectral analysis lies in constraining the temperature and density of the surrounding gas. However, leveraging line ratios of He-like ions provides a valuable avenue for temperature and density diagnostics or for establishing upper/lower limits on these parameters (Porquet et al., 2001). He-like ions emit three distinguishable lines: the forbidden line (z), the intercombination lines ($x + y$), and the resonance line (w) (Figure 1.5). Each of these lines corresponds to a specific energy level, with the relative strength of each feature dependent on the density (R ratio) and temperature of the gas (G ratio):

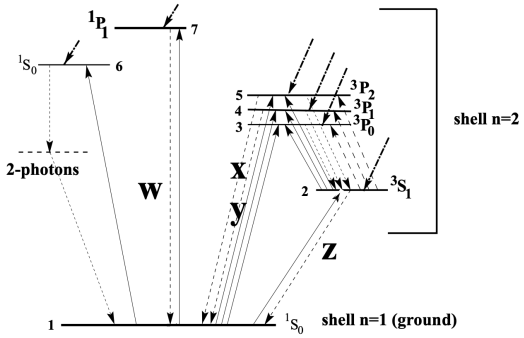

line	label	C V	N VI	O VII	Ne IX	Mg XI	Si XIII
resonance	w (r)	40.279	28.792	21.603	13.447	9.1681	6.6471
inter-	x	40.711	29.074	21.796	13.548	9.2267	6.6838
combination	y	40.714	29.076	21.799	13.551	9.2298	6.6869
forbidden	z (f)	41.464	29.531	22.095	13.697	9.3134	6.7394

Figure 1.4: Forbidden, intercombination, and resonance line energy levels scheme (left) and wavelengths of three of the main He-like ions X-ray lines (right). Taken from Porquet et al. (2001).

$$R = \frac{z}{x+y} = \frac{f}{i} \tag{1.2}$$

$$G = \frac{x+y+z}{w} = \frac{f+i}{r} \tag{1.3}$$

By taking the G and R ratios for the triplet, we can determine the temperature and the density of the gas, or at least place an upper or lower limit on their values (Figure 1.5).

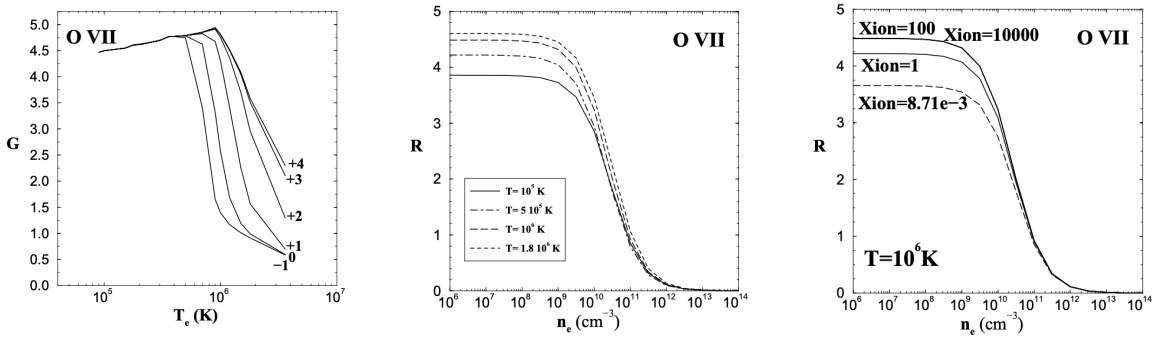

Figure 1.5: Temperature and density diagnostic plots for helium-like oxygen (OVII) ion triplet. Taken from Porquet and Dubau (2000).

From these ratios, the temperature and density of the gas can be inferred. Porquet and Dubau (2000) calculated density and temperature curves based on the G and R ratios. It is crucial to note that, at low values of R, we may effectively constrain density values, but challenges arise at higher R values, where we might only establish upper and lower limits on density. Similarly, for temperature, higher G values present challenges in constraining the temperature.

An essential consideration is that for the effective use of the G and R ratios, all three lines in the ion triplet must be detected, each with measurable equivalent widths to infer gas density and temperature. In some cases only one ratio could be obtained

to determine the G or R ratios

By employing the OVII triplet as a density diagnostic, Buhariwalla et al. (2023) successfully constrained the density of photoionized material within the AGN Mrk 1239 to a range of 10^5 and 10^{10} cm^{-3}. Utilising this density value, along with the known X-ray source luminosity and modeled ionization parameters, they further determined the relative location of the photoionized emitter to be a few parsecs (pc) from the supermassive black hole (SMBH), positioned no closer than the inner regions of the AGN torus.

High Resolution Spectral Analysis Tools

To analyse and model the components of AGN spectra, we must employ the use of spectral fitting tools, such as SPEX (Kaastra et al., 1996) and XSPEC (Arnaud, 1996). These software packages are optimised for the analysis of high resolution X-ray spectra, and adapted to modern X-ray observatories such as Chandra or XMM-Newton. They are capable of handling the fitting of multiple, highly complex, components simultaneously, making them an indispensable tool in studying AGN.

1.3 NGC 6814

NGC 6814 (z=0.0052) is categorized as a type 1.5 Seyfert AGN, exhibiting pronounced X-ray variability across various timescales, ranging from hours to days (Gallo et al., 2021). The optical and X-ray spectrum of NGC 6814 reveals moderate absorption features, indicating the presence of photoionized gas outflows within the AGN. Con-

sistent with other type 1.5 Seyferts, the X-ray spectrum features subtle excesses at both low and high energies, accompanied by narrow emission features in the Fe Kα band (Gallo et al., 2021).

1.3.1 2016 Observations

In 2016, NGC 6814 was observed using two instruments: the Swift X-Ray Telescope (XRT), alongside XMM-Newton. These observations contained an abnormal signature in the AGN flux. Upon analysis, detailed in Gallo et al. (2021), it was identified that the event corresponded to a rapid occultation (Figure 1.6). Such occurrences are likely common, but challenging to predict, making this instance one of the few where it was observed in its entirety. This unique observation provided an unprecedented opportunity for in-depth spectral analysis, offering insights into the nature of the occulting material.

1.3.2 The Nature of the Obscuring Material

Through modelling of the high-resolution spectra acquired from the XMM-Newton Reflection Grating Spectrometers (RGS) and the European Photon Imaging Camera (EPIC) p-n detector, Gallo et al. (2021) successfully extracted parameters of the obscuring gas. This included determining the column density, ionization state, and covering fraction, providing insights into key properties such as density, position, size, and velocity. The values of these parameters are documented in Table 1.1.

Given the brief duration of the occultation event, it is probable that the obscuring

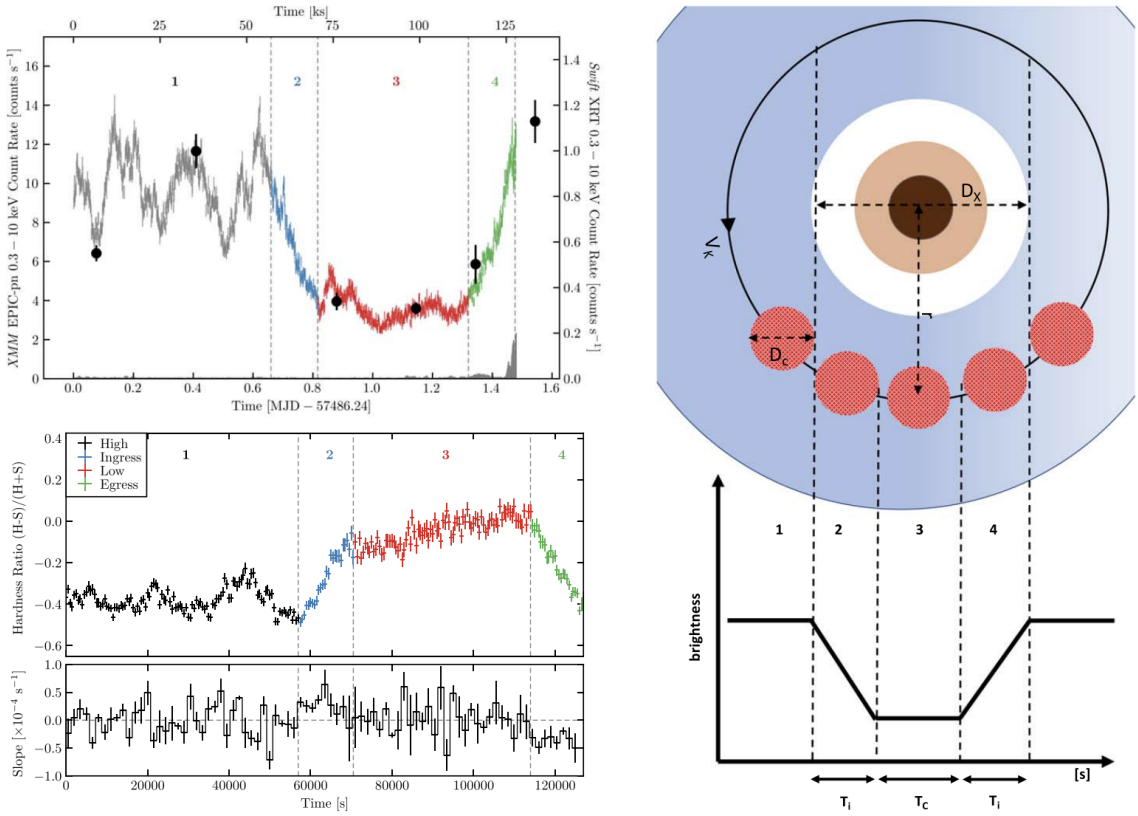

Figure 1.6: The light curve (top left), the hardness ratio curve (bottom left) demonstrating the eclipsing event in NGC 6814, and a schematic of the transient eclipsing event (right). Taken from Gallo et al. (2021).

gas was situated in close proximity to the SMBH. The fact that the flux did not reach zero indicates that the gas did not entirely cover the X-ray emitting region. Analysis further revealed that the obscurer was positioned at a distance of approximately $r \approx 2694 r_g = 4.34 \times 10^{15}$ cm, placing it within the broad-line region of NGC 6814.

1.3.3 2021 OBSERVATIONS

Gallo et al. (2021) determined that Seyfert 1.5s such as NGC 6814 make ideal candidates for capturing occultation events due to the observing angle - high enough to intercept the broad-line region and observe the occulting material, and low enough to

Model Parameter	Parameter Value
N_H	$(11.1 \pm 1.2) \times 10^{22}$ cm^{-2}
ξ	$(12.3^{+0.9}_{-3.8})$ erg s cm^{-1}
C_f (ingress and egress)	<0.01
C_f (maximum)	0.56 ± 0.2

Table 1.1: Reported parameters of the obscurer in NGC 6814. Taken from Gallo et al. (2021).

avoid being blocked by the torus. Further observations of NGC 6814 were taken with XMM-Newton in 2021 with the hopes of capturing another eclipsing event. During the analysis of the light curves, it was determined that there was no occultation event recorded in the observation.

1.4 MOTIVATION

While a second occultation event was not recorded in 2021, these data still provide a unique opportunity to probe the warm absorber in NGC 6814 and determine if the eclipsing gas observed in 2016 may originate from this region.

A similar approach to Di Gesu and Costantini (2016) will be employed to do so. By modelling the high resolution spectrum of the quasar 4C +74.26, Di Gesu and Costantini (2016) successfully identified the presence of at least one absorber, for which they found its column density, ionization parameter, and outflowing velocity. Kaastra et al. (2014) also outlines within their White Paper the feasibility of probing gas outflows in AGN using high resolution spectral data from observatories such as XMM-Newton or Chandra. Using simulations of NGC 4151, an intermediate type Seyfert galaxy similar to NGC 6814, they were able to model the spectrum in SPEX

(Kaastra et al., 1996) and detect the presence of at least five absorbers.

This thesis will include an in-depth analysis of the high resolution spectrum of NGC 6814, obtained from XMM-Newton RGS1 and RGS2 instruments. By fitting the absorption features in the spectrum of NGC 6814, we will obtain information on the warm absorber(s) in NGC 6814, and shed some light on the origins of the eclipsing material.

Chapter 2

OBSERVATIONS

Three observations of NGC 6814 were used for this project - Two observations with XMM-Newton starting 2016 April 8 for ∼130 ks and again starting 2021 October 01 for ∼123 ks, and one observation with Chandra starting 2021 August 2 for ∼57 ks (Table 2.1).

The XMM-Newton Observation Data Files (ODFs) were processed to produce calibrated event lists using the XMM-Newton Science Analysis System (SASV18.0.0). Light curves were extracted from these event lists to search for periods of high background flaring. These periods were neglected during analysis, but still resulted in reasonable length observations (∼112 ks). The RGS spectra were extracted using the SAS task RGSPROC and response matrices were generated using RGSRMFGEN. The spectra were optimally binned and the backgrounds were modelled.

The medium- and high-energy resolution transmission gratings (MEG and HEG, respectively) were used in combination with the ACIS CCD for the observation made with Chandra. The processed Chandra spectra were downloaded from the Chandra Transmission Grating Catalog and Archive[1]. For the analysis, the first-order (i.e. ±1) spectra were combined for both the MEG and the HEG.

Spectral fitting was performed using SPEX 3.07.03 and the fit quality is tested

[1]https://tgcat.mit.edu/

using the C-statistic, as the optimal binning allows bins to have a small number of counts since a Gaussian distribution cannot be assumed for these datasets. All parameters are reported in the rest frame of the source, unless specified otherwise. Figures remain in the observed frame unless specified otherwise. A value of Galactic column density toward NGC 6814 of 1.48×10^{21} cm^{-2} is adopted in all spectral fits with appropriate abundances (Willingale et al., 2013).

The total, unfitted spectrum is shown in Figures 2.1, 2.4, and 2.5, for 2021 (RGS), 2016 (RGS) and 2021 (Chandra), respectively. The 2016 RGS data are also divided to show the spectrum during the eclipsed phase (Figure 2.2) and the non-eclipsed phase (Figure 2.3).

Instrument	Date of Beginning of Observation	Exposure (s)
XMM-Newton RGS	2016-04-08 05:16:24	129940
XMM-Newton RGS	2021-10-01 13:28:34	123916
Chandra HETG	2021-08-02 00:30:15	56866.6

Table 2.1: Data Information for the 2021 Observation of NGC 6814

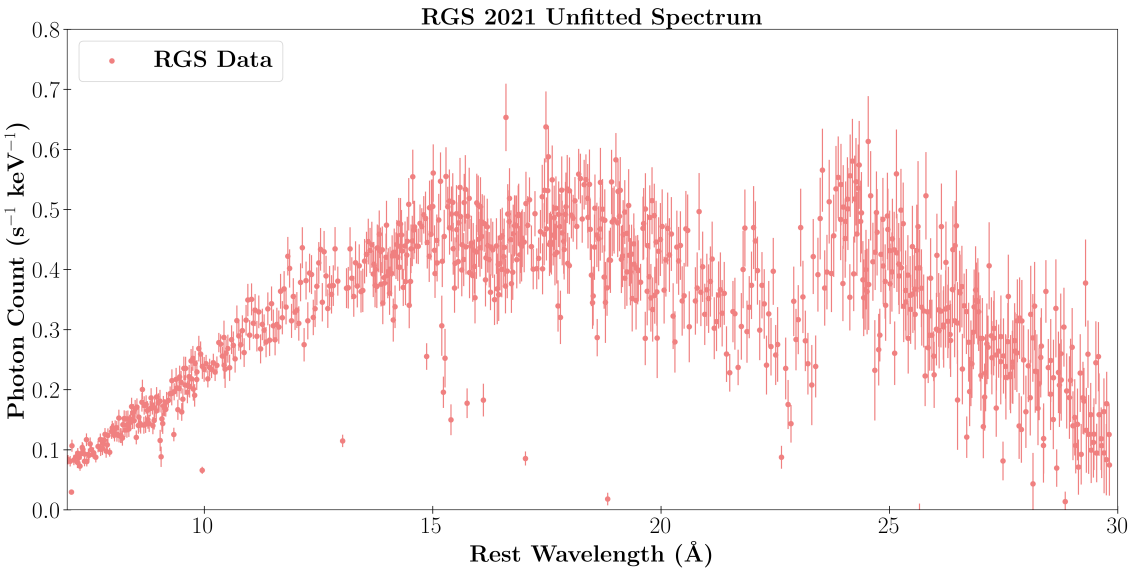

Figure 2.1: The unfitted 2021 XMM-Newton RGS spectrum.

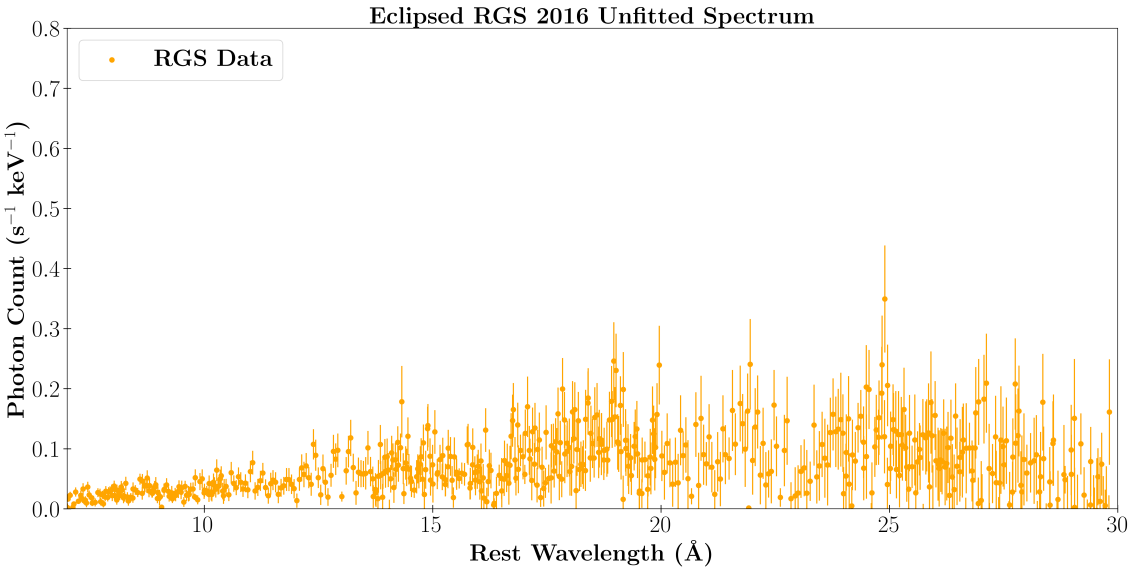

Figure 2.2: The unfitted 2016 XMM-Newton eclipsed RGS spectrum.

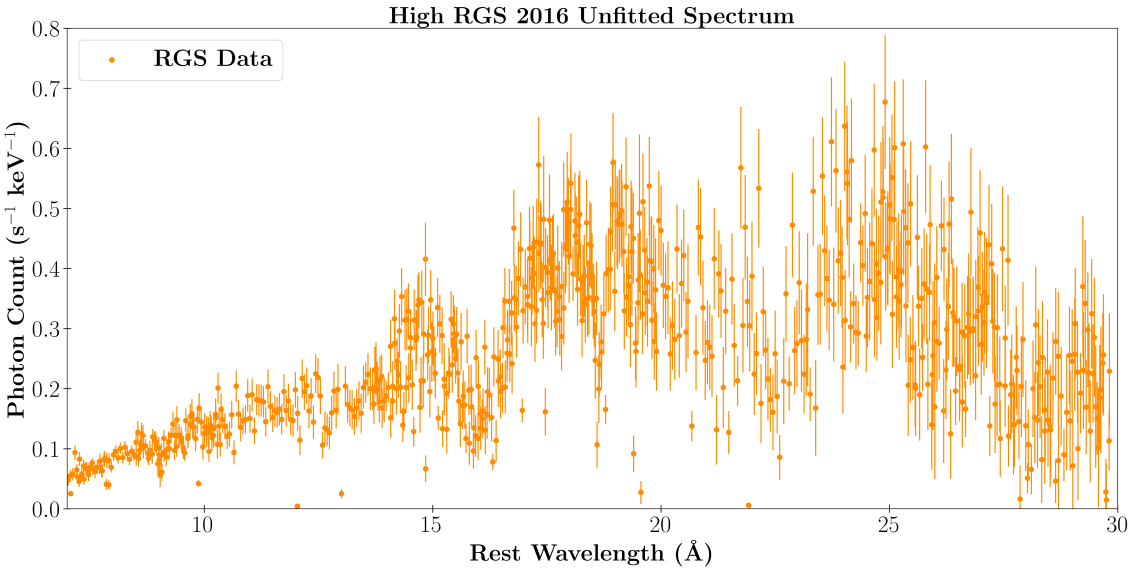

Figure 2.3: The unfitted 2016 XMM-Newton un-eclipsed RGS spectrum.

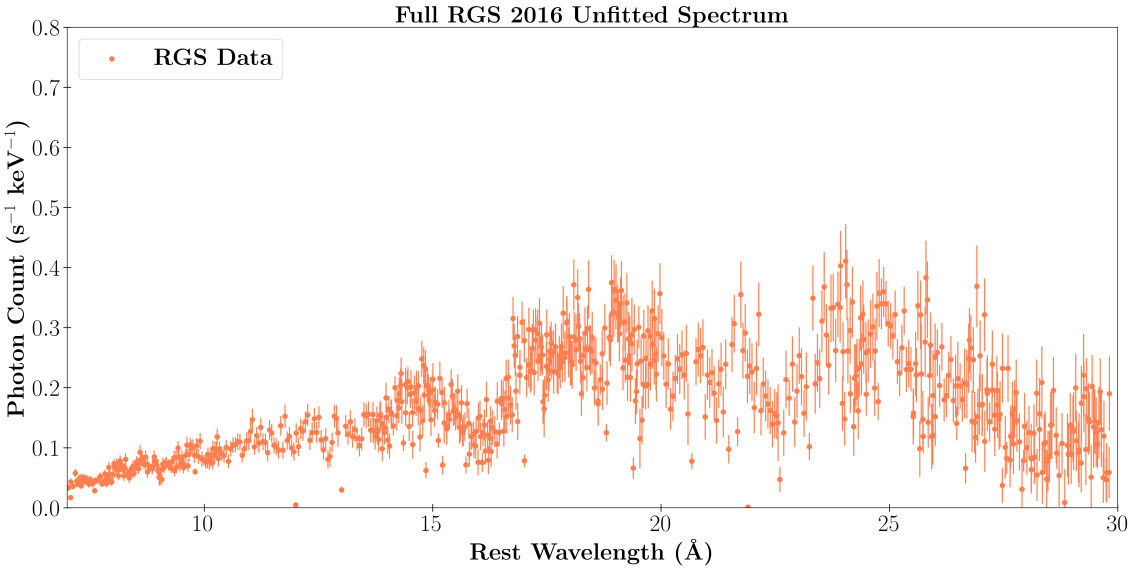

Figure 2.4: The unfitted 2016 XMM-Newton full RGS spectrum.

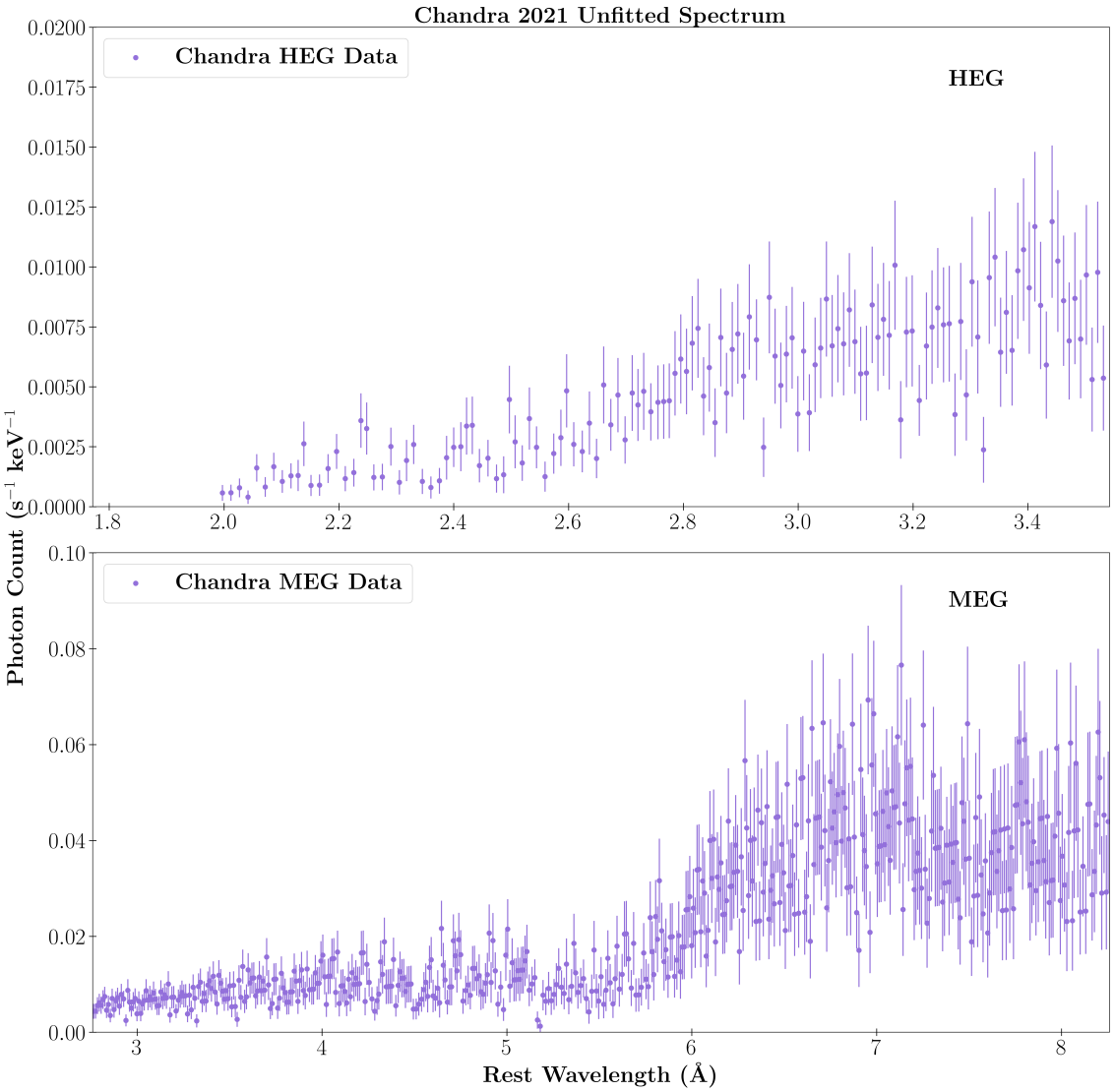

Figure 2.5: The unfitted 2021 Chandra HEG spectrum (top) and MEG spectrum (bottom).

Chapter 3

Line Search

As a preliminary step before implementing physical models on the spectrum, a line search was performed on the spectra to determine where the strongest features are located in the spectrum and identify them. In the interest of brevity, only the 2021 RGS data are examined at this time.

3.1 Methodology

All data analysis was performed using SPEX 3.07.03. Components to account for galaxy extinction and redshift were applied to the spectrum. A power law component was also fitted to the spectra to account for the primary emitter.

To perform the line search, a Gaussian component of fixed width and with normalisation set to zero but free to vary was added to the spectrum. A one-dimensional step grid search was performed. Starting at 7 Å, the Gaussian profile was fitted to the spectrum and the improvement over the power law continuum was recorded. The Gaussian would then take a step of 0.005 Å, and the fit process would repeat. This iteration continued over the entire 7-30 Å (Figures 3.1, 3.2). The step-size was selected to assure that narrow features would be captured and not skipped over in the step search. A change in the normalisation of the Gaussian profile would result in a C-statistic fit improvement. The strongest absorption and emission features accounting

for a 95% Akaike information criterion (AIC) certainty of detection ($\Delta C \geq 10$) were considered to be reliable detections and will be the focus of the line identification in the next section.

3.2 Line Identification

Seven emission and four absorption features were identified in the line search as being significant at the 95% level according to the AIC (see Section 3.1). The lines were identified using the AtomDB database[1]. The catalogue search was limited to lines with an emissivity greater than 10^{-17} photons cm^3 s^{-1} since it is unlikely that the data are sufficient to detect weaker features. It is also likely that the observed features will be shifted from the laboratory wavelength values in AtomDB. Consequently, we considered the strongest predicted feature (highest emissivity) nearest to the observed wavelength as being the most likely candidate. In Table 3.1, we list the spectral feature, the velocity shift, and the most likely chemical species that it originates from. If some lines have similar velocity shifts, they may originate from the same region around the central engine.

[1]http://www.atomdb.org/index.php

Emission or Absorption	ΔC	Line	Rest λ (Å)	Observed λ (Å)	Velocity Shift (km s^{-1})
Emission	13.04	Fe XXI	12.284	11.845	-7092
Emission	23.15	Fe XVIII	17.623	17.445	-1774
Emission	11.09	O VIII	18.973	19.020	6927
Emission	6.73	O VII (resonance)	21.602	21.700	1360
Emission	8.76	O VII (intercomb)	21.804	21.820	220
Emission	16.49	O VII (forbidden)	22.098	22.045	-719
Emission	10.36	Ca XIII	26.033	26.430	4571
Absorption	12.77	Fe XIX	16.780	16.305	-8487
Absorption	16.73	OVII	18.967	18.500	-7380
Absorption	12.37	Ca XV	22.730	22.770	528
Absorption	11.68	Ca XV	22.730	23.190	6067

Table 3.1: Line Identification of the 2021 XMM-Newton RGS data.

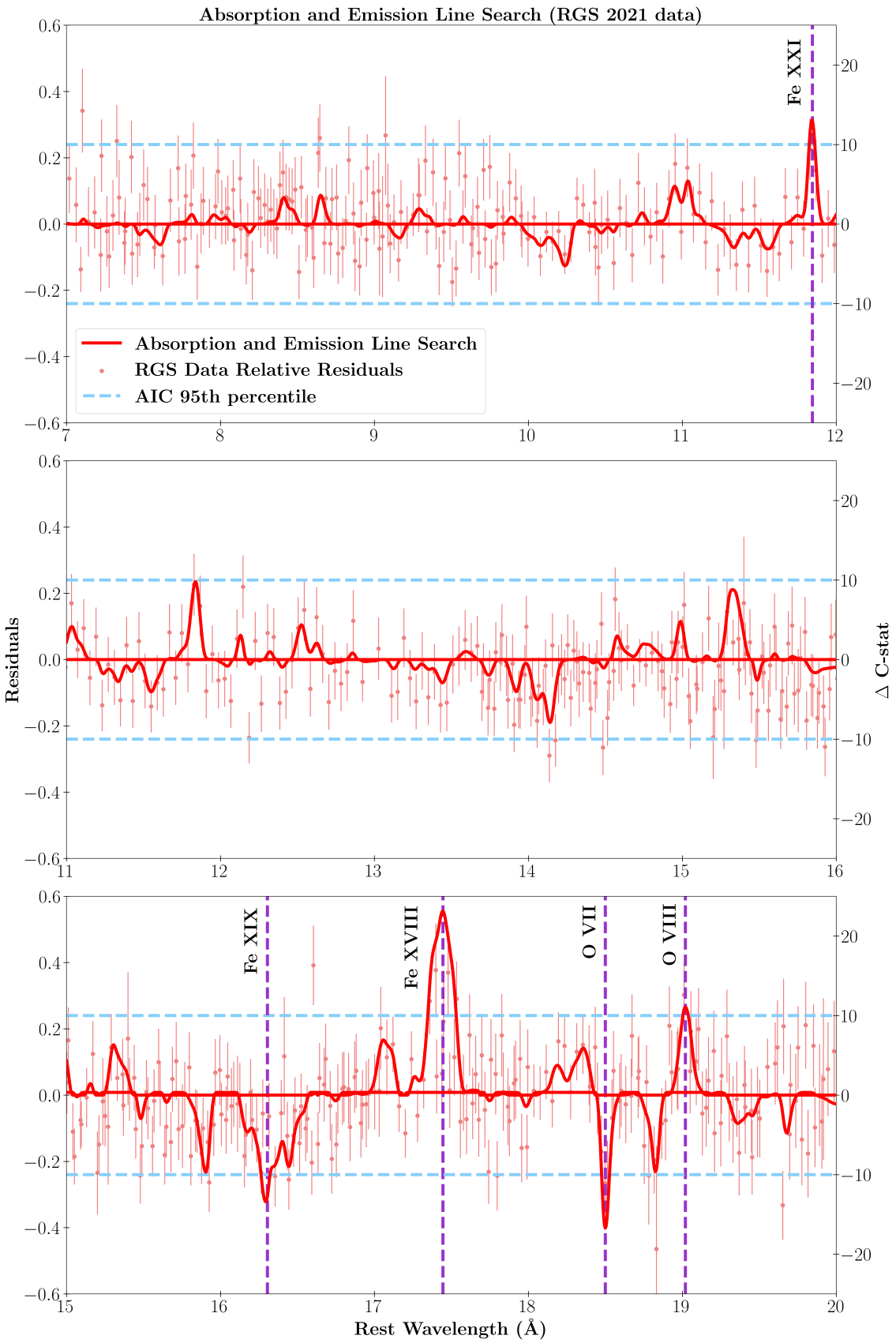

Figure 3.1: The line search conducted on the 2021 XMM-Newton RGS data from a range of 7-20 Å.

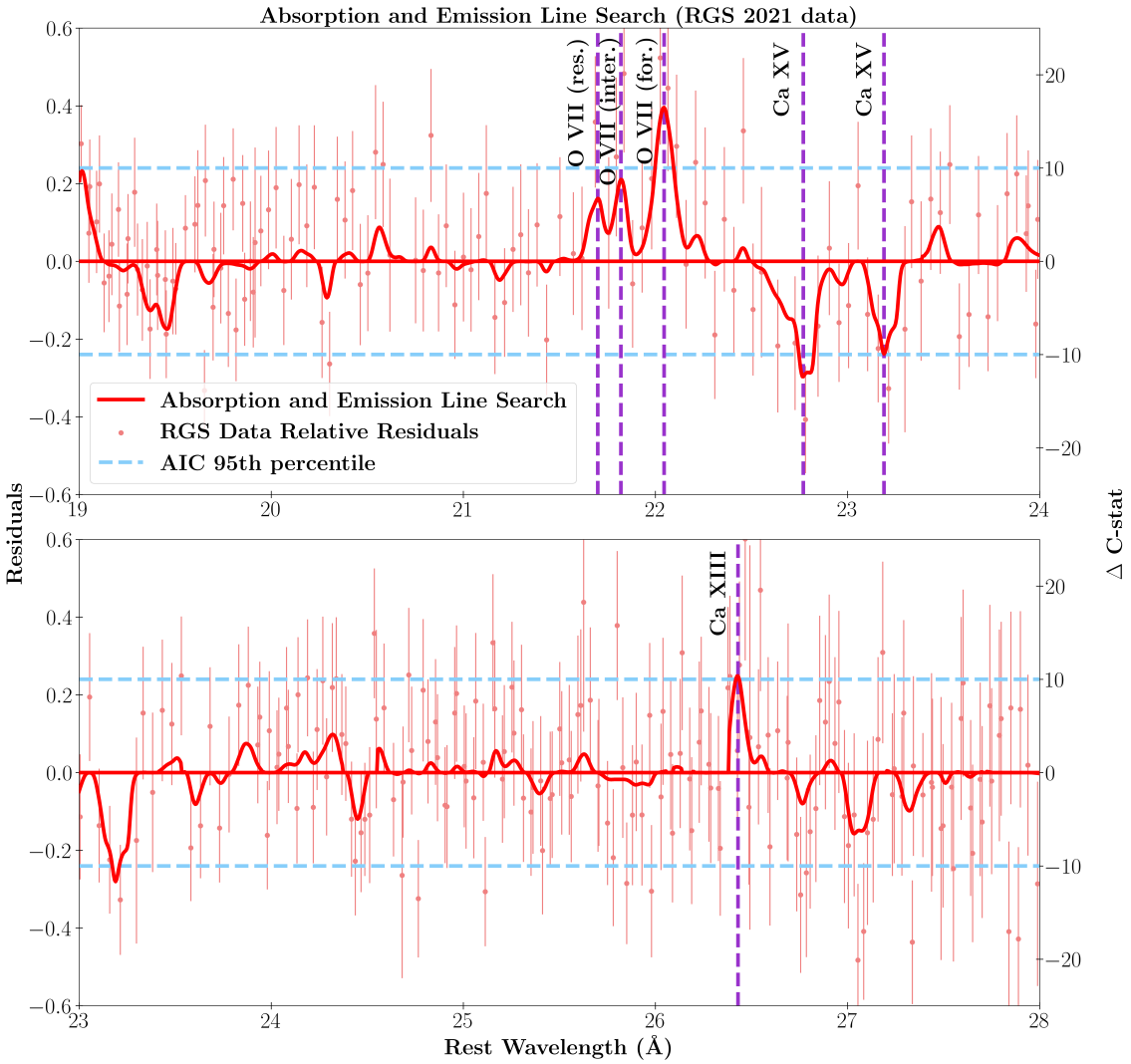

Figure 3.2: The line search conducted on the 2021 XMM-Newton RGS data from a range of 20-28 Å.

Chapter 4

Physical Models

In this chapter, we attempt to apply physically motivated models to describe the spectra of NGC 6814. From Chapter 3, we learned that ionised features are seen in absorption and emission, thus any model needs to account for both processes. The fits were all conducted on the XMM-Newton 2021 RGS spectrum in the interest of brevity, but the model will be compared to the 2016 data in Chapter 5.

4.1 Warm Absorption Models (xabs)

SPEX offers various options to model photo-ionised absorption, xabs being one of these models. Unlike other models on SPEX, the xabs model takes into account all relevant ions, and is less computationally intensive. The parameters of the model include:

- **Hydrogen Column density** (N_H) in units of 10^{28} m^{-2};
- **Ionisation Parameter** (ξ) in $\log_{10}$ form and in units of 10^{-9} Wm;
- **Covering Fraction** (fcov);
- **The Root Mean Square Velocity** (v) in units of km s^{-1};
- **The Velocity Distance** (dv) in units of km s^{-1};

- **The Average Systematic Velocity** (zv) in units of km s^{-1}, and;
- **Chemical Abundances for various elements.**

The spectral energy distribution (SED) given to the photo-ionised models was derived from fitting the average Swift 2022 spectrum along with the UVOT variability spectrum of NGC 6814 (Gonzalez et al., 2024). The spectra were fitted using the KYNSED model from Dovčiak et al. (2022), which includes X-ray emission from both the hot corona, and reflection due to disc illumination. The model assumes a colour-temperature correction of 1.7. Along with this, the model also requires a small disc truncation radius of $R_{out} = 200\ r_g$. While this SED is not derived from data that are contemporaneous with the 2021 RGS spectrum, it is more accurate and does result in a better fit than the default SED provided by SPEX.

4.2 2021 RGS Fit

Warm Absorber 1

Before attempting to fit a first absorber to the spectrum, a two-dimensional step grid search was performed to determine at what ionisation and systematic velocity resulted in a significant fit improvement.

The step grid search revealed three regions that yielded a good fit improvement. Each region was tested and fitted to determine which resulted in the best fit. The central region at $\log(\xi\ ) \approx 3$ and $zv \approx -2500$ km s^{-1} was found to be the region that resulted in the best fit and was implemented to the model (Figure 4.1).

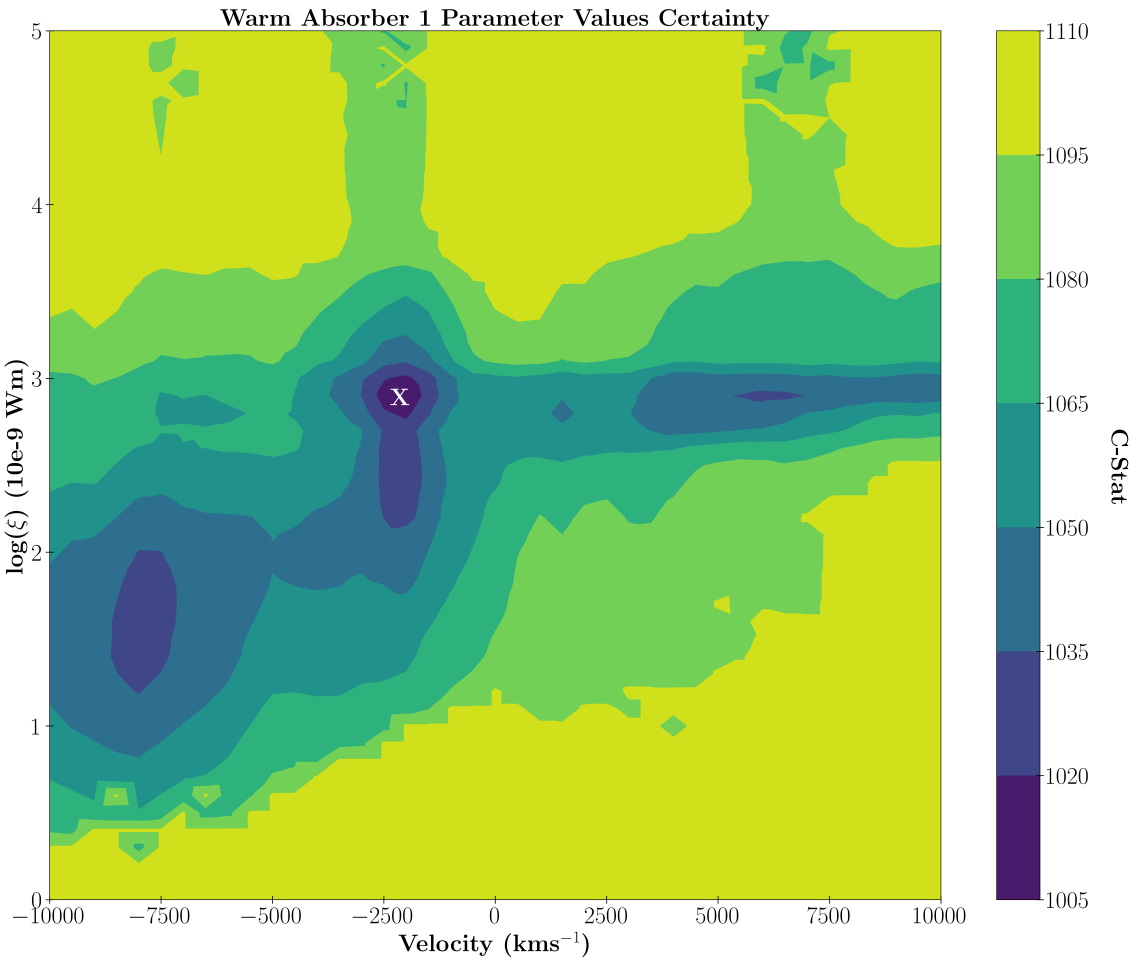

Figure 4.1: The step grid search performed to determine the ionisation and systematic velocity of the first warm absorber. The central region at $\log(\xi) \approx 3$ and $zv \approx -2500$ km s^{-1} was found to be the region that resulted in the best fit.

The first warm absorber mainly fitted the absorption features at higher energies (< 16 Å). The single warm absorber model resulted in a C-statistic of 1001.94 with 6 free parameters and 829 degrees of freedom, resulting in an AIC value of 1013.041 and a relative likelihood of 99.999% compared to the power law model.

Warm Absorber 2

After fitting the first warm absorber to the spectrum, there were still some features that remained to be fitted at lower energies (> 16 Å). A second step grid search was conducted to determine if a second warm absorber would result in a statistical fit improvement, and to attempt to fit the remaining absorption features.

The second step grid search revealed that there was still a region at $\log(\xi) \approx 2.5$ and $zv \approx -2500$ km s^{-1} that would yield a fit improvement (Figure 4.2). When a second absorber with similar ionisation and systematic velocity was added to the model and fitted, the ionisation parameters adjusted slightly so that $\log(\xi_1) \approx 2.98$ and $\log(\xi_2) \approx 2.35$. The second warm absorber fitted the prominent absorption features at ≈ 16 Å, but did not fit the absorption features at lower energies.

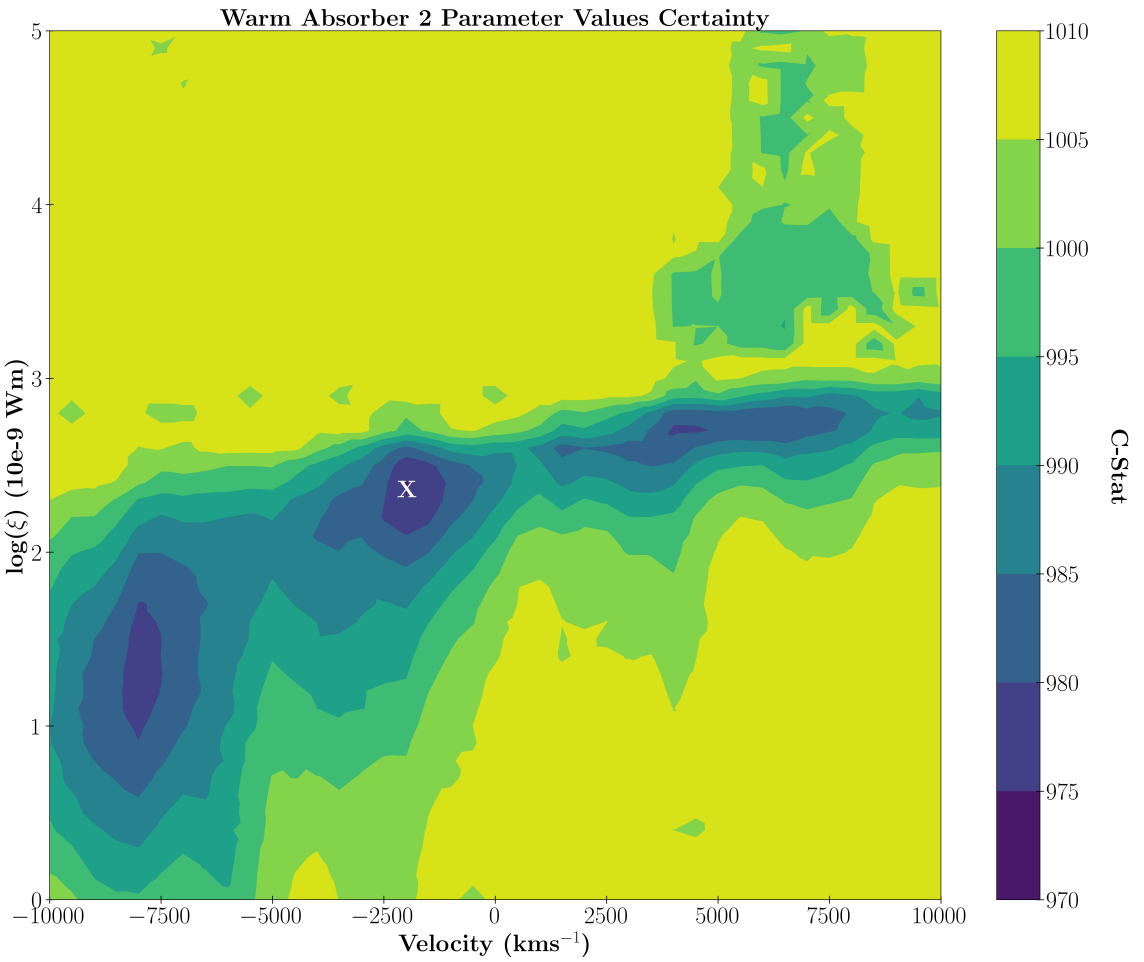

Figure 4.2: The step grid search performed to determine the ionisation and systematic velocity of the second warm absorber.

Warm Absorber Model

The two warm absorber model resulted in a C-statistic of 974.90 with 10 free parameters and 825 degrees of freedom, resulting in an AIC value of 994.167 and a relative likelihood of 99.203% compared to the single warm absorber model.

The transmission curves of each absorber revealed that each absorber fitted different areas of the spectrum (Figure 4.3). The first warm absorber fitted mainly features in the higher energy band, while the second warm absorber fitted a larger feature at around 16 Å and features at lower energies. However, some features above 17 Å remain unfitted. Statistically, a third warm absorber is not required. It is possible that with a more accurate SED, features at lower energies may be fitted by this model. The free parameters and errors of the various components are reported in Table 4.1, and the complete fit to the data is shown in Figure 4.4.

Model Parameter	**Parameter Value**
pow	
norm	$5.85\ ^{+0.80}_{-0.81}$E+06
gamma	$2.08\ ^{+0.02}_{-0.02}$
xabs 1	
N_H (10^{28}m^{-2})	$2.13\ ^{+1.63}_{-0.62}$E-03
$log(\xi)$ (10^{-9}Wm))	$2.98\ ^{+0.04}_{-0.04}$
v (km s^{-1})	$20.98\ ^{+21.45}_{-10.91}$
zv (km s^{-1})	$-2251.20\ ^{+287.31}_{-206.61}$
xabs 2	
N_H (10^{28}m^{-2})	$4.79\ ^{+1.04}_{-0.98}$E-04
$log(\xi)$ (10^{-9}Wm))	$2.36\ ^{+0.10}_{-0.09}$
v (km s^{-1})	$45.53\ ^{+34.78}_{-29.17}$
zv (km s^{-1})	$-2131.70\ ^{+605.53}_{-120.40}$

Table 4.1: Free parameters of the absorption model for the 2021 RGS data of NGC 6814.

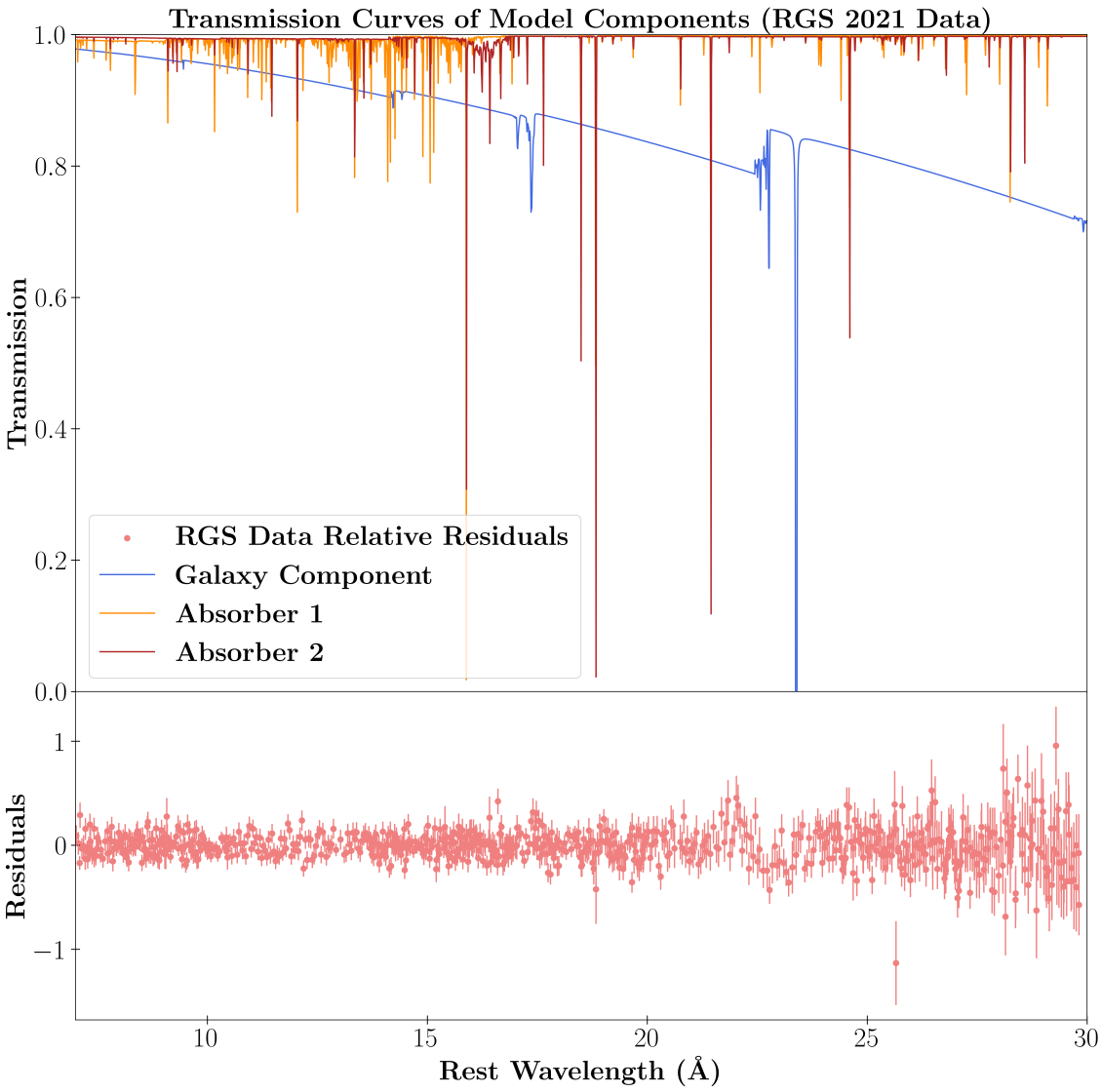

Figure 4.3: The transmission curves of components in the fitted model on the XMM-Newton 2021 RGS spectrum (top) and residuals (bottom). Warm Absorber 1 contributes mainly to fitting lines at higher energies, while Warm Absorber 2 contributes mainly to fitting absorption features at 15-16 Å and other features at lower energies that remained unfitted with only one absorber.

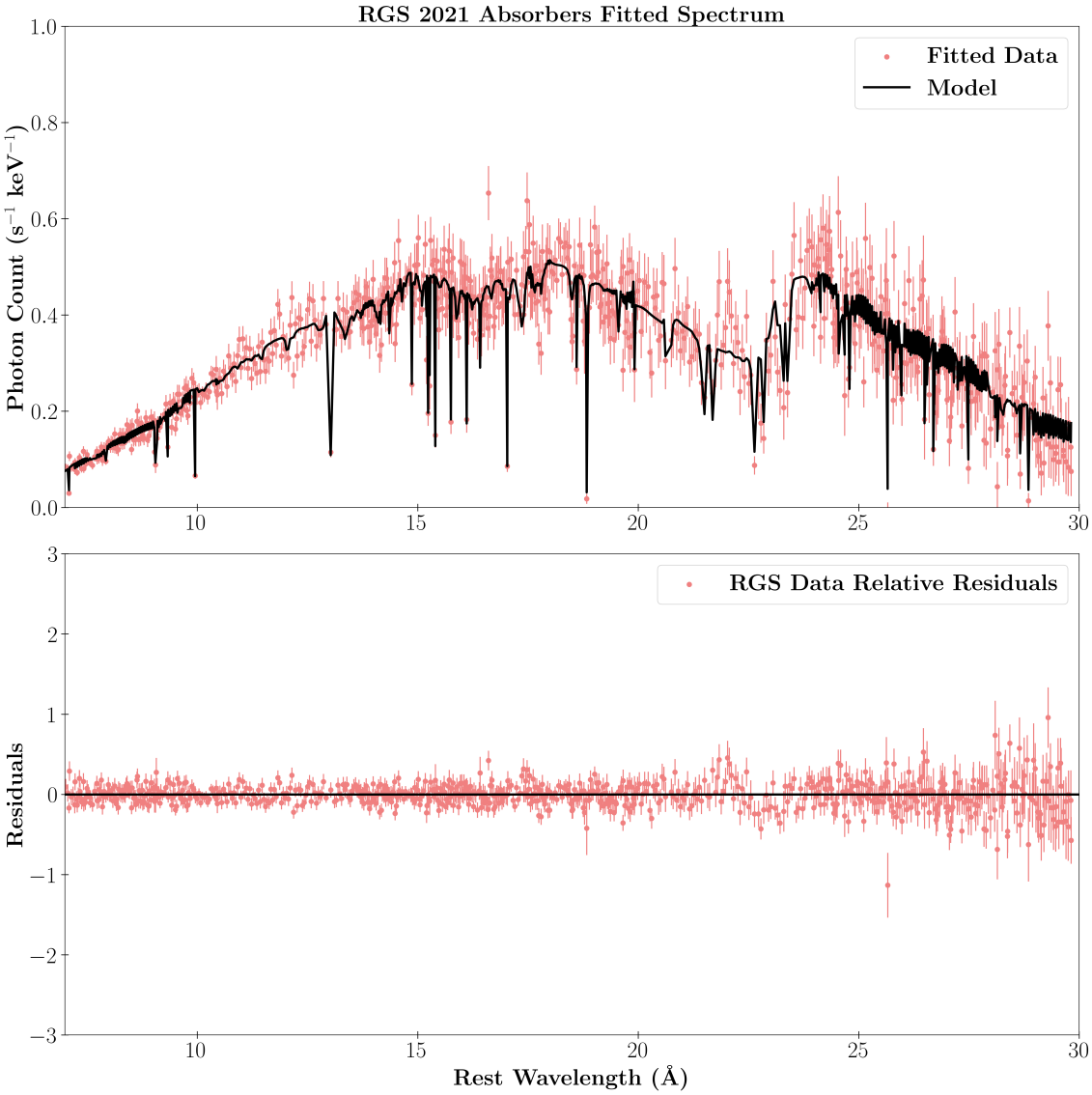

Figure 4.4: The modelled 2021 XMM-Newton RGS spectrum (top) and residuals (bottom).

Chapter 5

Discussion

5.1 Comparison of the 2021 RGS Model to the 2016 RGS Data

For a simple analysis, the 2021 model found in Chapter 4 was compared to the 2016 data that contained the eclipse. To maintain the parameter of the warm absorber, the model was refitted leaving only the power law normalisation and index (Γ) factor, and both warm absorber column densities free to vary (Figure 5.1).

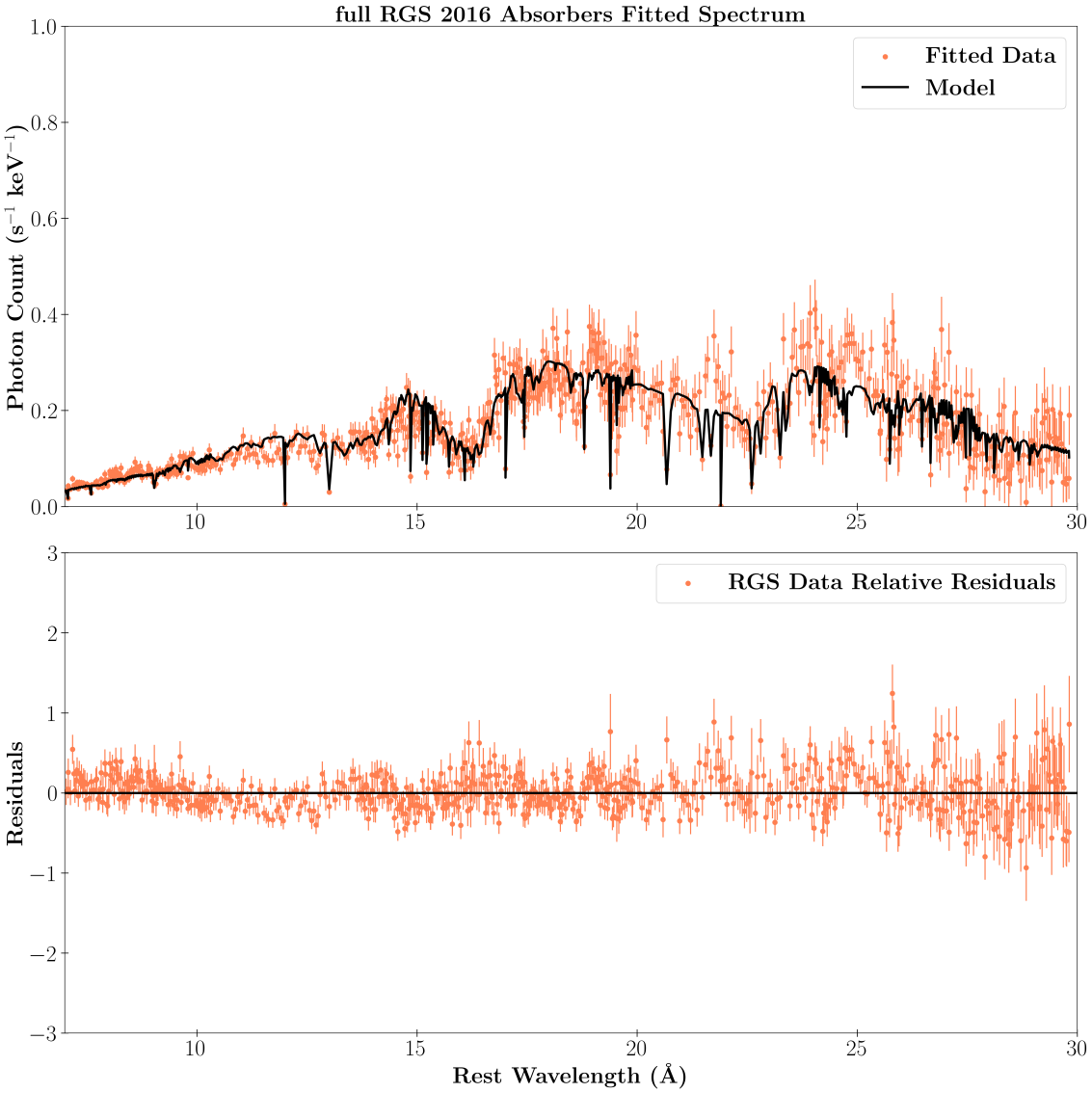

Figure 5.1: The 2021 WA model fitted to the 2016 XMM-Newton full RGS spectrum. The 2021 WA model has been modified in power law normalisation and photon index, and columns densities of WA1 and WA2 (top). The residuals of the fit are shown in the bottom panel.

Overall, the model fits the 2016 reasonably well. The power law normalisation and gamma factor parameters both were comparable to the values obtained from the 2021 fitting (Table 5.1). However, the column density parameters from both warm absorbers increased by an order of magnitude. This suggests a possible connection between the warm absorber in NGC 6814 and the obscuring gas observed in 2016.

Knowing that the 2021 model fits the 2016 absorption well, further analysis must be done to connect both spectra. Examination will investigate the SED during 2016 as well as the changes in both WAs. It will also investigate the eclipse spectrum exclusively to determine if the WAs might also be the eclipsing material.

Model Parameter	**Parameter Value**
pow	
norm	$4.22\ ^{+0.09}_{-0.09}$E+06
gamma	$2.18\ ^{+0.03}_{-0.03}$
xabs 1	
N_H (10^{28}m^{-2})	$2.46\ ^{+0.18}_{-0.18}$E-02
$log(\xi)$ (10^{-9}Wm))	2.98
v (km s^{-1})	20.98
zv (km s^{-1})	-2251.20
xabs 2	
N_H (10^{28}m^{-2})	$3.99\ ^{+0.28}_{-0.27}$E-03
$log(\xi)$ (10^{-9}Wm))	2.36
v (km s^{-1})	45.53
zv (km s^{-1})	-2131.70

Table 5.1: Free parameters of the absorption model added to the 2016 full RGS data of NGC 6814. The power law normalisation and gamma factor, and both warm absorber column densities were free to vary.

5.2 A Picture of the Warm Absorption System in NGC 6814

The parameters found for the two warm absorber components contain clues on the distribution of clouds in the central region. Knowing that the first warm absorber (WA1) is at a higher ionisation and column density, but similar systematic velocity to the second warm absorber (WA2) suggests that both clouds may be a part of the same system moving together. WA1 may be located closer to the corona, explaining its higher ionisation, and absorbing a portion of the X-rays before they reach other regions of the cloud, such as WA2. It is also possible that even one cloud may be embedded in the other, or that they may both be embedded in a larger system.

While the emission components were not modelled yet, there were also emission lines visible in the spectra, meaning that there is at least one emitting region outside the observer's line of sight and scattering X-rays. It is interesting to speculate that this emitter might be the same material as the WAs, but located out of the line-of-sight.

Further analysis is required to solidify these claims. However, Figure 5.2 provides a preliminary idea of how the surrounding gas is distributed within the central region of NGC 6814. Here, we describe WA1 and WA2 as being two components of the same medium moving outwards at a velocity of ≈ 2500 km s^{-1}. It could be that the two WAs that we find actually describe an ionisation and density gradient within the same cloud (Figure 5.2).

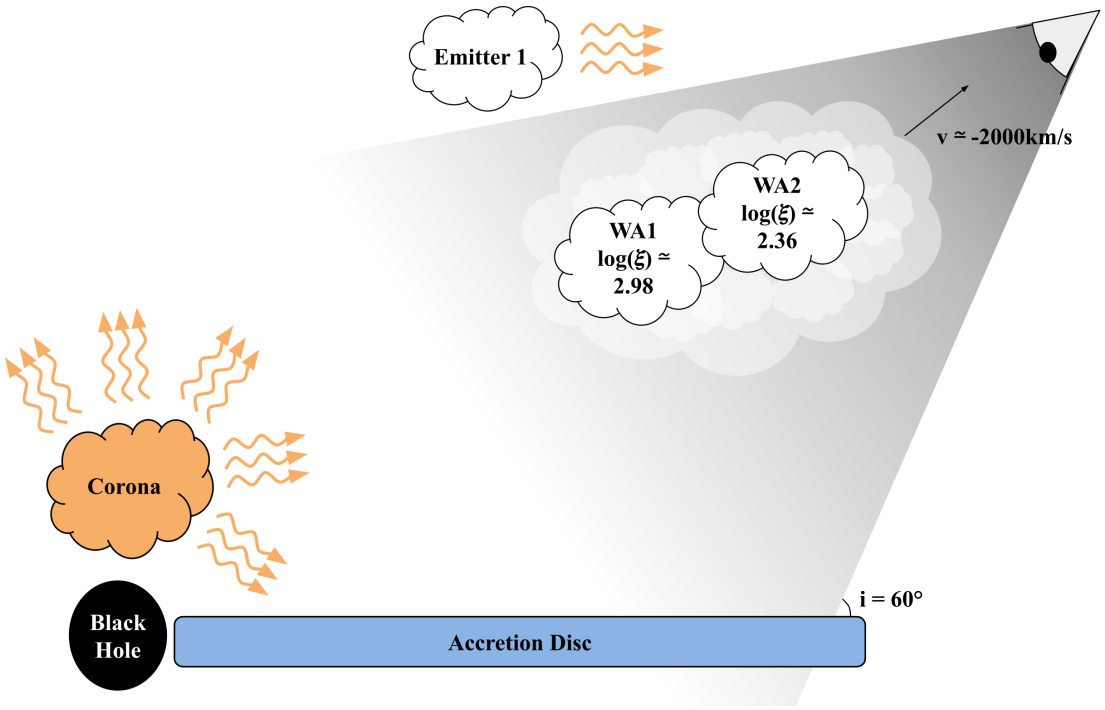

Figure 5.2: A Picture of the Warm Absorption System in NGC 6814.

This illustration is reminiscent of the conclusions drawn from Pottie et al. (2023), where it was deduced that the obscurer observed in 2016 was not the result of a single homogeneous obscuring cloud, rather a complex system of clouds embedded within a highly ionised halo. Further analysis is required to determine if the properties observed in the warm absorber modelled in the 2021 observation match the properties of the obscurer. However, these are exciting results that shed some light on how the surrounding gas in NGC 6814 is distributed.

Chapter 6

Conclusions

The goal of this work was to model the warm absorber in the XMM-Newton RGS 2021 spectrum of NGC 6814. During this work, we:

- Performed a line search on the XMM-Newton RGS 2021 spectra;
- Identified seven emission and four absorption features in the XMM-Newton RGS 2021 spectrum and their velocity shifts;
- Performed a step grid search through the ionisation and velocity shift on the XMM-Newton RGS 2021 spectrum;
- Found two warm absorbers in the XMM-Newton RGS 2021 spectrum;
- Modelled the warm absorbers in the XMM-Newton RGS 2021 spectrum;
- Fitted the model to the XMM-Newton RGS 2016 full spectrum;
- Qualitatively compared the fits on the XMM-Newton RGS 2021 spectrum and on the RGS 2016 full spectrum, and;
- Pictured how the central region of NGC 6814 may appear.

When fitted to the XMM-Newton 2016 observations, the model yielded a good fit to the data. However further work should be done to determine if this is the best fit we can obtain for the data.

As both warm absorber components are moving at similar velocities and have comparable ionisations, it can be deduced that these components may be a part of a larger inhomogenous cloud system with varying densities and ionisation levels. These results are reminiscent of those found in Pottie et al. (2023) where it was determined that the obscurer observed in NGC 6814 in 2016 was the result of multiple clouds embedded within an ionised halo.

Further analysis of NGC 6814 is required to fully understand this complex system. Future work includes:

- Modelling the photoionised emitter(s) in the XMM-Newton RGS 2021 spectrum;
- Fitting the model using a more accurate SED;
- Fitting the complete model to the XMM-Newton RGS 2016 eclipsed, un-eclipsed, and full spectra;
- Modelling the Chandra HETG 2021 spectrum;
- Make an in-depth comparison between the 2016 and 2021 spectra of NGC 6814 and compare the obscurer observed in 2016 to the warm absorber observed in 2021, and;
- Determine whether the obscurer observed in 2016 may have originated from the warm absorber of NGC 6814.

Bibliography

K. A. Arnaud. XSPEC: The First Ten Years. In George H. Jacoby and Jeannette Barnes, editors, *Astronomical Data Analysis Software and Systems V*, volume 101 of *Astronomical Society of the Pacific Conference Series*, page 17, January 1996.

Margaret Z. Buhariwalla, Luigi C. Gallo, J. Mao, S. Komossa, J. Jiang, A. Gonzalez, and D. Grupe. The collisional and photoionized plasma in the polarized NLS1 galaxy Mrk 1239. , 521(2):2378–2390, May 2023.

L. Di Gesu and E. Costantini. The warm absorber in the radio-loud quasar 4C +74.26. , 594:A88, October 2016.

M. Dovčiak, I. E. Papadakis, E. S. Kammoun, and W. Zhang. Physical model for the broadband energy spectrum of X-ray illuminated accretion discs: Fitting the spectral energy distribution of NGC 5548. , 661:A135, May 2022.

Luigi C. Gallo. Revealing the Innermost Regions of Active Galaxies. , 105(4):143, August 2011.

Luigi C. Gallo, Adam G. Gonzalez, and Jon M. Miller. Eclipsing the X-Ray Emitting Region in the Active Galaxy NGC 6814. , 908(2):L33, February 2021.

Luigi C. Gallo, Jon M. Miller, and Elisa Costantini. Active galactic nuclei with high-resolution X-ray spectroscopy. *arXiv e-prints*, page arXiv:2302.10930, February 2023.

A. G. Gonzalez, L. C. Gallo, J. M. Miller, E. S. Kammoun, A. Ghosh, and B. A. Pottie. Characterizing X-ray, UV, and optical variability in NGC 6814 using high-cadence Swift observations from a 2022 monitoring campaign. , 527(3):5569–5579, January 2024.

Mark Henry Jones, Lambourne Robert J A., and Stephen Serjeant. *An introduction to galaxies and Cosmology*. Cambridge University Press, 2 edition, 2015.

J. S. Kaastra, R. Mewe, and H. Nieuwenhuijzen. SPEX: a new code for spectral analysis of X & UV spectra. In *UV and X-ray Spectroscopy of Astrophysical and Laboratory Plasmas*, pages 411–414, January 1996.

J. S. Kaastra, Y. Terashima, T. Kallman, Y. Haba, E. Costantini, L. Gallo, Y. Fukazawa, F. Tombesi, N. Anabuki, H. Awaki, G. Brown, L. di Gesu, K. Ebisawa, J. Ebrero, M. Eckart, K. Hagino, K. S. Long, J. Miller, T. Miyazawa, S. Paltani, C. Reynolds, C. Ricci, H. Sameshima, H. Seta, Y. Ueda, and M. Urry. ASTRO-H White Paper - AGN Winds. *arXiv e-prints*, page arXiv:1412.1171, December 2014.

D. Porquet and J. Dubau. X-ray photoionized plasma diagnostics with helium-like ions. Application to warm absorber-emitter in active galactic nuclei. , 143:495–514, May 2000.

D. Porquet, R. Mewe, J. Dubau, A. J. J. Raassen, and J. S. Kaastra. Line ratios for helium-like ions: Applications to collision-dominated plasmas. , 376:1113–1122, September 2001.

B. Pottie, L. C. Gallo, A. G. Gonzalez, and J. M. Miller. A colourful analysis: Probing the eclipse of the black hole and central engine in NGC 6814 using X-ray colour-colour grids. , 525(3):3633–3644, November 2023.

Barbara Sue Ryden and Bradley M. Peterson. *Foundations of Astrophysics*. Cambridge University Press, 2021.

R. Willingale, R. L. C. Starling, A. P. Beardmore, N. R. Tanvir, and P. T. O'Brien. Calibration of X-ray absorption in our Galaxy. , 431(1):394–404, May 2013.